An *LCC* Wireless Charger With Embedded Cell Equalization via a Shared Compensation Inductor

Pengcheng Zhang, *Senior Member, IEEE*, Tianhao Zhang, Xinjie Yu, *Senior Member, IEEE*, Zhaoyang Yuan, *Member, IEEE*, Changsong Cai, *Senior Member, IEEE*, Hongjian Lin, *Senior Member, IEEE*, Yefei Xu, *Member, IEEE*, and Lizhou Liu, *Member, IEEE*

***Abstract*—This article presents an integrated approach for achieving simultaneous battery charging and balancing in wireless power transfer (WPT) systems, unifying both functions within a single, compact circuit topology. The proposed design repurposes the receiver-side compensation inductor as the primary winding of a multiwinding transformer, enabling the balancing function to be realized without introducing additional magnetic components or control circuits. Balancing voltages and accurate intercell energy redistribution are governed by the transformer's turns ratio, allowing precise regulation without auxiliary converters or switch matrices. Consequently, the system avoids the multiple receiver coils and complex switching networks typical of conventional WPT equalizers, leading to notable reductions in cost, volume, and control complexity. Furthermore, the topology ensures accurate balancing without stringent coupling consistency and remains stable under coil misalignment, highlighting its robustness to mutual inductance variations. These attributes make the system particularly suitable for dynamic or mobile energy storage applications. Experimental results validate the proposed equalizer, demonstrating a charging efficiency of 81.5% at a 19 W load while maintaining intercell voltage deviations below 0.02 V. These results demonstrate that the proposed method offers a compact, reliable, and scalable approach for integrated battery management in WPT-enabled systems.**

***Index Terms*—Battery balancing, misalignment tolerance, wireless power transfer (WPT).**

Received 12 May 2025; revised 25 July 2025; accepted 5 September 2025. Date of publication 16 September 2025; date of current version 19 January 2026. This work was supported in part by the National Natural Science Foundation of China under Grant 52207010, Grant 62401379, and Grant 52407014, in part by the Young Elite Scientists Sponsorship Program of the China Association for Science and Technology (CAST) under Grant YESS20220659, and in part by the Natural Science Foundation of Sichuan Province under Grant 2025ZNSFSC1237. Recommended for publication by Associate Editor C. K. Lee. *(Corresponding author: Lizhou Liu.)*

Pengcheng Zhang and Xinjie Yu are with the Department of Electrical Engineering and the State Key Laboratory of Power System, Tsinghua University, Beijing 100083, China (e-mail: pczhang@tsinghua.edu.cn; yuxj@tsinghua.edu.cn).

Tianhao Zhang, Yefei Xu, and Lizhou Liu are with the School of Electrical Engineering, Sichuan University, Chengdu 610065, China (e-mail: 2022141440186@stu.scu.edu.cn; xuyefei@scu.edu.cn; liulizhou@scu.edu.cn).

Zhaoyang Yuan and Changsong Cai are with the School of Electrical Engineering and Automation, Wuhan University, Wuhan 430072, China (e-mail: zhaoyangyuan@whu.edu.cn; changsongcai@whu.edu.cn).

Hongjian Lin is with the Department of Electrical and Computer Engineering, University of Alberta, Edmonton, AB T6G 2R3, Canada (e-mail: hongjian_lin@ieee.org).

Color versions of one or more figures in this article are available at https://doi.org/10.1109/TPEL.2025.3610102.

Digital Object Identifier 10.1109/TPEL.2025.3610102

I. Introduction

WIRELESS power transfer (WPT) has emerged as a transformative solution for powering autonomous and unattended systems, including applications such as long-range drones operating in remote or inaccessible environments [1]. By enabling contactless and automated energy replenishment, WPT effectively extends mission duration and reduces the dependence on manual intervention. However, the demanding operational conditions and frequent charge–discharge cycles inherent in such applications accelerate the development of battery voltage imbalances within the energy storage system [2]. These imbalances significantly compromise energy utilization, system performance, and safety, posing increasing challenges as battery pack sizes grow and charge–discharge rates become more aggressive. Consequently, a reliable cell balancing mechanism is crucial for mitigating these issues and ensuring the stability, safety, and optimal performance of energy storage systems in WPT-powered autonomous applications [3].

To address the challenge of maintaining consistent cell voltage, various active balancing techniques have been developed. These methods redistribute energy from cells with higher states of charge to those with lower states, thereby improving pack capacity utilization and extending lifespan. Balancing systems are generally categorized into two primary approaches, standalone and integrated balancing systems [4].

Standalone balancing systems operate independently of the main charge–discharge circuit, often utilizing external components, such as inductors [5], capacitors [6], [7], [8], or switch matrices [9], to transfer energy between cells during various operating states [10]. While these systems provide flexibility in design and control, they often require multiple switches and peripheral components. These limitations are especially problematic in compact, weight-sensitive applications, such as WPT-powered applications, where minimizing weight and volume is critical for optimal performance [11].

In contrast, integrated balancing systems embed the balancing function into the power conversion stage, reducing hardware overhead and simplifying the overall design [12]. By exploiting voltage or current ripples in the converter stage, or using multiwinding transformers, these integrated systems reduce the number of components required, improving efficiency and compactness [13], [14]. As WPT systems inherently involve high-frequency power conversion, integrating the balancing function

within the WPT architecture has emerged as a promising approach [15]. Examples of such designs include multireceiver WPT systems that use multiple secondary coils to achieve uniform voltage outputs [16], voltage multipliers that regulate multiple ports [17], and switch-matrix-based designs that enhance scalability and current throughput [18]. Multicoil systems, in particular, have been proposed to address the scalability and high-voltage demands of WPT charging and balancing systems, offering a potential solution for handling larger battery packs and higher power levels.

Despite these advances, multicoil systems often struggle with performance degradation under practical conditions, such as coil misalignment or geometric inconsistencies. Maintaining uniform coupling between coils in real-world environments is challenging, and variations in mutual inductance can result in unequal voltage outputs and inefficient balancing [19], [20]. To address these challenges, Zhang et al. [21] proposed a dual-layer structure that facilitates both intragroup and intergroup balancing, enhancing misalignment tolerance, although precise coil parameter matching remains a requirement. Alternatively, single-coil configurations reduce hardware redundancy but often reintroduce switching elements, complicating the circuit design and control.

Motivated by the demand for compact, scalable, and misalignment-tolerant balancing architectures in WPT-based energy systems, this paper proposes a novel scheme that repurposes the receiver-side compensation inductor to implement integrated cell balancing. This approach eliminates additional magnetic components and control circuitry, resulting in a simplified and robust system architecture.

The salient aspects of this work are summarized as follows.

1) The receiver-side compensation inductor is repurposed as the primary winding of the equalization transformer, eliminating any standalone balancing transformer and its high-frequency driver. By exploiting the intrinsic high-frequency excitation of the WPT link, the design reduces magnetic parts, volume, and cost.
2) Energy redistribution is regulated solely by the transformer turns ratio on the shared core. This single-core topology maintains accurate balancing despite coupling variations and spatial misalignment, avoiding the sensitivity typical of multicoil schemes.
3) Unlike multireceiver and conventional transformer-based designs that dedicate one coil to each cell, the proposed architecture supports two additional cells with only one extra secondary winding, thus reducing the coil count by half while keeping the diode configuration unchanged. This plug-and-play expansion streamlines the construction of large battery packs.

The rest of this article is organized as follows. Section II introduces the proposed integrated equalization scheme and details its operating principle. Section III presents the experimental prototype and analyzes its performance, including experimental validation of voltage balancing, efficiency, and robustness. Section IV provides a comparative analysis and discussion against existing WPT-based balancing circuits across key performance metrics. Finally, Section V concludes this article.

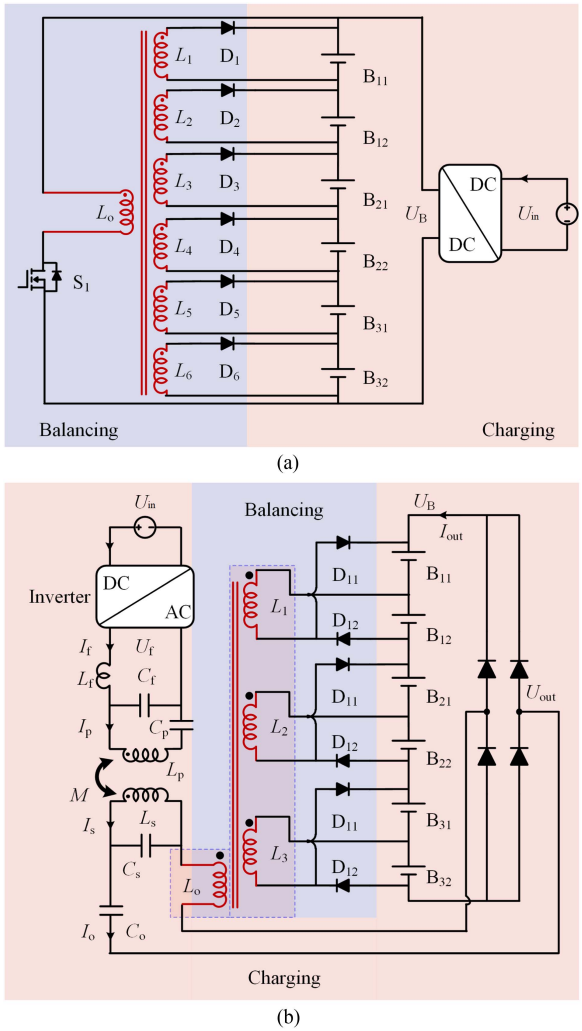

Fig. 1. Schematic diagrams of two charging and equalization architectures. (a) Conventional architecture with separate transformer-based equalization. (b) Proposed WPT-based architecture integrating charging and equalization via a shared compensation inductor.

II. Proposed Integrated Equalization Scheme Using Shared Compensation Inductor

Fig. 1(a) depicts a conventional transformer-based equalization architecture. In this configuration, battery cells B_{11}–B_{32} are charged from a dc source U_{in} via the circuit on the right side. The equalizer, positioned on the left, employs a single primary winding realized by inductor L_o and six dedicated secondary windings, each corresponding to an individual cell. An inverter S_1 provides high-frequency ac to L_o, facilitating magnetic energy transfer to each cell through its respective winding. While this architecture achieves effective balancing, the requirement for multiple isolated magnetic paths increases the system's volume and complexity, particularly in space and weight constrained WPT applications.

A. Operating Principle

The proposed WPT-based equalizer, as shown in Fig. 1(b), integrates the balancing function into the receiving-side Inductor-Inductor-Capacitor (LCC) compensation network. This is

achieved by repurposing the receiving-side compensation inductor L_o to serve as the primary winding of a multiwinding balancing transformer. This eliminates the need for a separate equalization transformer or additional dedicated high-frequency power source for balancing.

The system's primary side is driven by an ac source U_f through a compensation network (L_f, C_f, L_p, and C_p). Energy is magnetically coupled to the secondary coil L_s and processed by the secondary-side *LCC* compensation network (C_s, L_o, and C_o). This network is designed to ensure a constant current (CC) output at the resonant frequency f.

A core innovation involves repurposing the compensation inductor L_o on the receiving-side *LCC* network. This inductor serves a dual purpose. It functions as part of the *LCC* resonant circuit for WPT power transfer. Simultaneously, it acts as the primary winding for a multiwinding balancing transformer. The high-frequency ac power across L_o is derived directly from the WPT flow. Half-bridge rectifiers are connected to the secondary windings of L_o to perform energy redistribution. Each rectifier balances two adjacent cells. By leveraging the shared compensation inductor, the proposed design reduces the number of secondary windings required for balancing by half compared to the conventional architecture in Fig. 1(a), thereby enhancing circuit compactness and integration.

B. Balancing Principle of the WPT-Based Equalizer

Mode I [$nT \sim nT + \frac{T}{2}$]*:* Fig. 2(a) depicts the circuit behavior in Mode I. During this half-cycle, the inverter conducts in the backward direction, driving the primary resonant network (C_f, L_f, C_p, and L_p). Magnetic coupling transfers energy to the receiving coil L_s, inducing the secondary current I_s. This current passes through the secondary resonant components (C_s, L_o, and C_o) and the rectifier, charging the battery string and contributing to the output current I_{out}. Simultaneously, during this half cycle, the voltage across the repurposed inductor L_o acts as the primary for the multiwinding balancing transformer. Energy is coupled to the secondary windings L_1–L_3, denoted as L_n. The voltage induced in secondary winding L_n drives a balancing current to the even-indexed cell B_{n2} through its associated diode D_{n2}.

Mode II [$nT + \frac{T}{2} \sim (n+1)T$]*:* Fig. 2(b) shows the operation in Mode II, where the inverter commutates and conducts in the reverse direction. The primary side operates identically to Mode I. On the secondary side, the reversed polarity of the voltage across L_o couples energy to the secondary windings L_1–L_3, driving a balancing current to the odd-indexed cell B_{n1} through its associated diode D_{n1}.

To facilitate analysis, the secondary-side equivalent circuit is presented in Fig. 3. The charging resistance of the battery string is

$$R_0 = \frac{U_{out} + 2U_D}{I_{out}} \tag{1}$$

where U_{out} is the string terminal voltage and U_D is the forward voltage drop of each rectifier diode.

Waveforms shown in Fig. 4 corroborate the preceding analysis. The output voltage U_{out} alternates between two levels at $t = T/2$ and $t = T$, corresponding to Modes I and II operation.

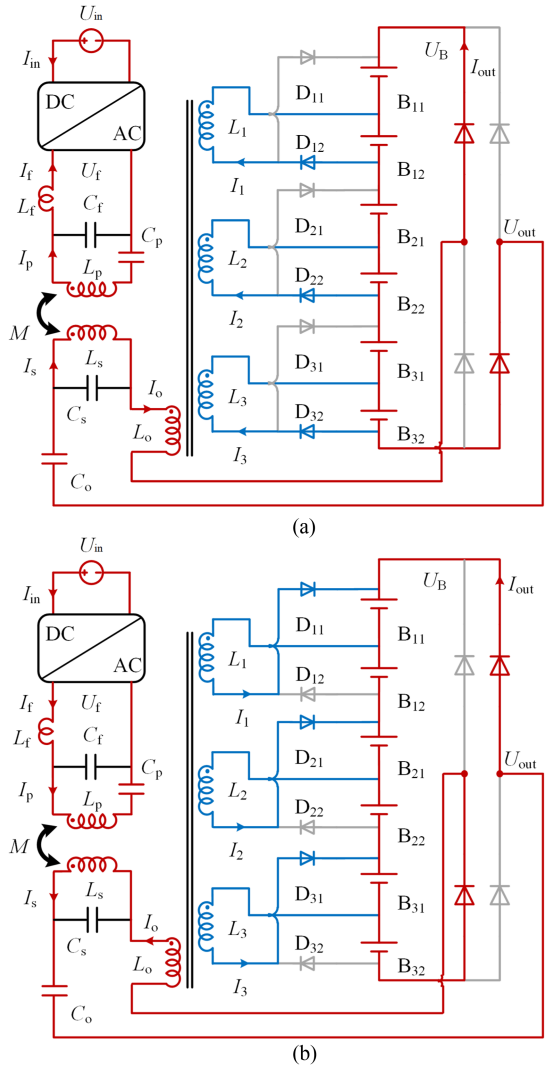

Fig. 2. System operating conditions under different modes: (a) Mode I and (b) Mode II.

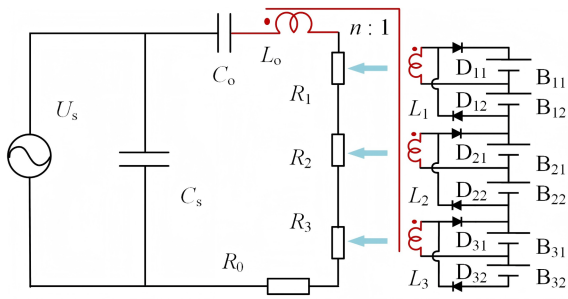

Fig. 3. Equivalent resistances referred to the receiving coil: charging resistance R_0 and balancing resistances R_1, R_2, and R_3.

The balancing currents I_1–I_3 appear as unidirectional pulses with varying amplitudes, reflecting the initial voltage differences among the corresponding cells, larger imbalances result in higher current magnitudes. This voltage-dependent behavior demonstrates effective passive balancing without additional control complexity. For illustration purposes, the current amplitudes

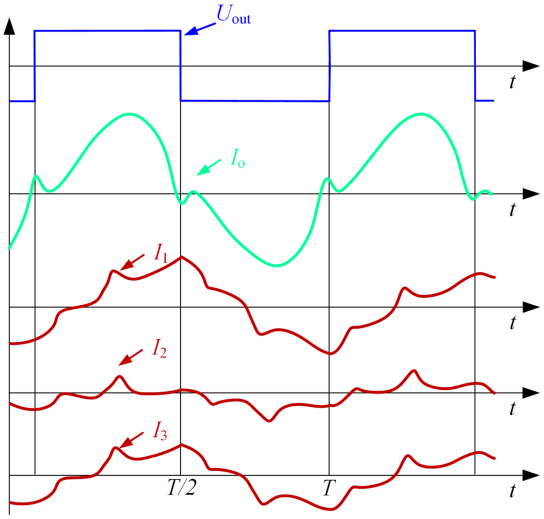

Fig. 4. Balancing operation of the proposed circuit for the energy storage cells.

in Fig. 4 are exaggerated to highlight this principle. In practical operation, the waveforms converge as the cell voltages become balanced.

Analytical expressions for the balancing current, power, and equivalent resistance in each mode are derived. In Mode I, the balancing current for battery B_{n2} is denoted as I_{n_I} and can be expressed as

$$I_{n\_\mathrm{I}} = \frac{U_{L_\mathrm{o}}/n - U_{\mathrm{D}_{n2}} - U_{\mathrm{B}_{n2}}}{R_{L_n}} \tag{2}$$

where U_{L_o} is the terminal voltage of the inductor L_o, n is the transformer turns ratio, $U_{\mathrm{D}_{n2}}$ is the forward voltage drop across diode D_{n2}, $U_{\mathrm{B}_{n2}}$ is the terminal voltage of battery B_{n2}, and R_{L_n} represents the equivalent internal resistance of the inductor L_n.

The power consumption of this balancing loop in Mode I, denoted as P_n, is given by

$$P_{n\_\mathrm{I}} = \left(\frac{\frac{U_{L_\mathrm{o}}}{n} - U_{\mathrm{D}_{n2}} - U_{\mathrm{B}_{n2}}}{R_{L_n}}\right) \cdot \frac{U_{L_\mathrm{o}}}{n}. \tag{3}$$

Referred to the output side, the equivalent resistance becomes

$$R_{\mathrm{n\_I}} = \frac{P_{n\_\mathrm{I}}}{I_{\mathrm{out}}^2}. \tag{4}$$

In Mode II, the balancing current of cell B_{n2} is

$$I_{n\_\mathrm{II}} = \frac{-\frac{U_{L_\mathrm{o}}}{n} - U_{\mathrm{D}_{n2}} - U_{\mathrm{B}_{n2}}}{R_{L_n}} \tag{5}$$

with power dissipation

$$P_{n\_\mathrm{II}} = \left(\frac{-\frac{U_{L_\mathrm{o}}}{n} - U_{\mathrm{D}_{n2}} - U_{\mathrm{B}_{n2}}}{R_{L_n}}\right) \cdot \frac{U_{L_\mathrm{o}}}{n} \tag{6}$$

and equivalent resistance

$$R_{n\_\mathrm{II}} = \frac{P_{n\_\mathrm{II}}}{I_{\mathrm{out}}^2}. \tag{7}$$

The effective voltage U_{L_o} originates from a symmetrical ac excitation, and the transformer turns ratio n is fixed across

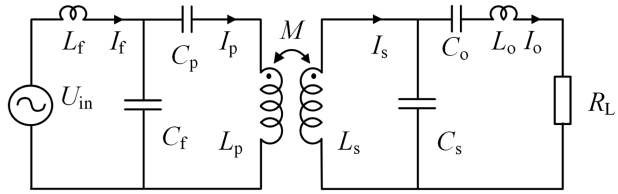

Fig. 5. Equivalent circuit of the WPT system.

modes. Since identical components are used in both modes, the balancing currents I_{n_I} and I_{n_II} are mainly determined by the corresponding cell voltages $U_{\mathrm{B}_{n1}}$ and $U_{\mathrm{B}_{n2}}$. A higher cell voltage reduces the potential difference across the conduction path, thereby lowering the resulting balancing current. This enables voltage-dependent energy redistribution and effective cell balancing without the need for additional control circuitry.

C. Operating Principle of the WPT System

Fig. 5 illustrates the employed compensation network topology, which is a structural variation of the standard *LCC–LCC* network. A key difference lies on the secondary side, where C_o is positioned closer to L_o than in a symmetric *LCC* configuration. This arrangement enables more flexible tuning, particularly with respect to the transformer-side inductance L_o, which typically requires greater design freedom. Although the structure introduces asymmetry, the network preserves the fundamental operating principles of a symmetric *LCC–LCC* topology. As a result, it retains the key advantages of the *LCC* configuration, zero-phase-angle operation across a wide load range, inherent CC output behavior, and ease of gain tuning through discrete component selection.

To analytically verify these claimed characteristics, particularly the CC output behavior, we apply the fundamental harmonic approximation. Assuming that the system is perfectly tuned to the operating angular frequency $\omega = 2\pi f$ such that the following resonance conditions are met:

$$\begin{cases} \omega L_\mathrm{f} = \frac{1}{\omega C_\mathrm{f}}, & \omega L_\mathrm{s} = \frac{1}{\omega C_\mathrm{s}} \\ \omega L_\mathrm{p} - \frac{1}{\omega C_\mathrm{f}} = \frac{1}{\omega C_\mathrm{p}}, & \omega L_\mathrm{o} - \frac{1}{\omega C_\mathrm{o}} = \frac{1}{\omega C_\mathrm{s}}. \end{cases} \tag{8}$$

The reactive impedance components of each resonant tank are effectively canceled, resulting in a purely resistive impedance at the operating frequency. By treating the power coils L_p and L_s as an ideal transformer with mutual inductance $M = k\sqrt{L_\mathrm{p}L_\mathrm{s}}$ and applying Kirchhoff's voltage law to the resonant network under these conditions, the branch currents at the fundamental frequency can be deduced as

$$\begin{cases} I_\mathrm{f} = \frac{M^2 U_\mathrm{in} R_\mathrm{L}}{\omega^2 L_\mathrm{f}^2 L_\mathrm{s}^2} \\ I_\mathrm{p} = -\mathrm{j}\frac{U_\mathrm{in}}{\omega L_\mathrm{f}} \\ I_\mathrm{s} = \frac{M U_\mathrm{in} R_\mathrm{L}}{\omega^2 L_\mathrm{f} L_\mathrm{s}^2} \\ I_\mathrm{o} = -\mathrm{j}\frac{M U_\mathrm{in}}{\omega L_\mathrm{f} L_\mathrm{s}}. \end{cases} \tag{9}$$

Specifically, the expression for the output current delivered to the rectifier, corresponding to I_o in (9), is independent of the equivalent load resistance R_L. This analytical result confirms the inherent CC output characteristic predicted by the topology.

The rectifier converts the ac current I_o into dc power, operating with an ac input voltage U_{out}. The resulting dc output voltage is applied to the energy-storage cells. The relationship between this voltage, the cell string voltage U_B, and the diode voltage drop is as follows:

$$U_{out} = U_B + 2U_{AD} + 2R_{AD}I_{DC} \tag{10}$$

where U_{AD} and R_{AD} are the forward voltage drop and dynamic resistance of each diode, respectively, and I_{DC} denotes the magnitude of the dc output current, ideally proportional to the rms value of the *AC* current I_o from (9).

D. System Efficiency and Loss Analysis

The overall system efficiency is evaluated by considering both the power delivered for charging the battery string and the energy redistributed among unbalanced cells through the embedded equalizer. The total effective output power therefore consists of two components, direct charging power and balancing power. Based on this, the system efficiency is defined as

$$\eta = \frac{U_B I_o + \sum_{n=1}^{n}\sum_{m=1}^{m} U_{nm} I_n}{U_{in} I_{in}} \tag{11}$$

where U_B and I_o represent the voltage and current delivered to the battery string. U_{nm} and I_n are the voltage and balancing current of the mth cell in module n. U_{in} is the dc input voltage of the inverter and I_{in} is the primary-side resonant inductor current.

To elucidate the underlying factors governing the system's energy conversion efficiency, this section establishes a comprehensive theoretical loss model. The objective of this model is not to provide a quantitative breakdown, which is challenging due to the inherent difficulty in accurately measuring high-frequency pulsed currents, but rather to offer a qualitative analysis of the principal loss mechanisms. This analysis serves as a crucial theoretical framework for guiding high-efficiency design and parameter optimization. The total system loss is decomposed into four primary components: inverter loss P_i, balancing circuit loss P_B, main rectifier loss P_R, and resonant network conduction loss P_{res}.

The inverter loss P_i within the full-bridge inverter originate from three distinct phenomena: MOSFET body–diode conduction P_{condD}, switching transitions P_{SWMOS}, and ON-state conduction $P_{condMOS}$. The body–diode loss is formulated as

$$P_{condD} = \frac{2\sqrt{2}}{\pi} U_f I_{in} \left(1 - \sin\left(\frac{\varphi_p}{2}\right)\right) + \frac{1}{\pi} r_D I_{in}^2 \left(\pi - \varphi_p - \sin\varphi_p\right) \tag{12}$$

where U_f and r_D are the diode's threshold voltage and equivalent ON-state resistance, I_{in} is the inverter input current, and φ_p is the phase angle of the input equivalent impedance. The switching loss is given by

$$P_{SWMOS} = \sqrt{2} U_{in} I_f \cos\left(\frac{\varphi_p}{2}\right) f_{sw} \left(\frac{E_{SWON} + E_{OFF}}{U_R I_R} + \frac{Q_{RR}}{I_{RD}}\right) \tag{13}$$

where E_{SWON} and E_{OFF} are the turn-ON/OFFenergy loss parameters, U_R and I_R are the reference voltage and current for those parameters, Q_{RR} is the reverse recovery charge, and I_{RD} is the reference current for the reverse recovery characteristics. The ON-state conduction loss is determined by

$$P_{condMOS} = \frac{1}{\pi} r_{DS} I_{in}^2 (\pi - \varphi_p - \sin\varphi_p) \tag{14}$$

where r_{DS} is the MOSFET's ON-state resistance.

The power loss in the embedded balancing circuit, P_B, is a composite of resistive losses in the windings and diode forward voltage drops

$$P_B = \sum_{n=1}^{N}\sum_{m=1}^{M} (I_{nm}^2 r_{nm} + I_{nm} U_D) + \sum_{n=1}^{N} I_n^2 r_n \tag{15}$$

where r_{nm} is the resistance of the balance loop, U_D is the diode's forward voltage drop, I_{nm} is the balancing current for cell B_{nm}, I_n is the current in winding L_n, and r_n is the resistance of winding L_n.

Finally, the losses from the main power path include the rectifier loss, P_R, and the conduction loss, P_{res}. The rectifier power loss is expressed as

$$P_R = 2I_{out} U_D \tag{16}$$

where U_D is the forward voltage drop of the rectifier diodes. The conduction loss is given by

$$P_{res} = I_p^2 r_T + I_s^2 r_R \tag{17}$$

where I_p and I_s are the rms currents in the primary and secondary resonant tanks, and r_T and r_R are the equivalent series resistances of the primary and secondary resonant networks, respectively.

The complex dependencies on phase angle φ_p and the functional form of the current, as captured in (12)–(14), reveal that inverter efficiency is highly sensitive to the resonant condition and any deviation from soft-switching operation. Likewise, (17) mathematically confirms that the quality factor of the resonant tanks, which is inversely related to their equivalent series resistance, is a fundamental determinant of the WPT efficiency. Therefore, this model provides the theoretical foundation that explains the efficiency characteristics observed in Section III and validates the component selection strategy for the experimental prototype.

III. Prototype Design, Implementation, and Performance Analysis

A prototype equalizer was initially developed and evaluated using a string of six Ultracapacitor (UC) cells (CHP5R5L405R-TWX, 5.5V/4F) to enable swift experimental validation, particularly due to their inherent rapid charging characteristics. Subsequent to the UC validation, the system's performance was additionally verified with battery strings. The physical realization of the prototype is illustrated in Fig. 6.

The equalizer's primary-side topology featured a full-bridge inverter, implemented with N-channel MOSFETs (IRF3205, 55V/110A). Rectification was accomplished utilizing MBR20100CT diodes, complemented by SSB43L-E3/52T diodes within the rectifier stage. A dedicated voltage acquisition system was employed for the real-time monitoring and recording

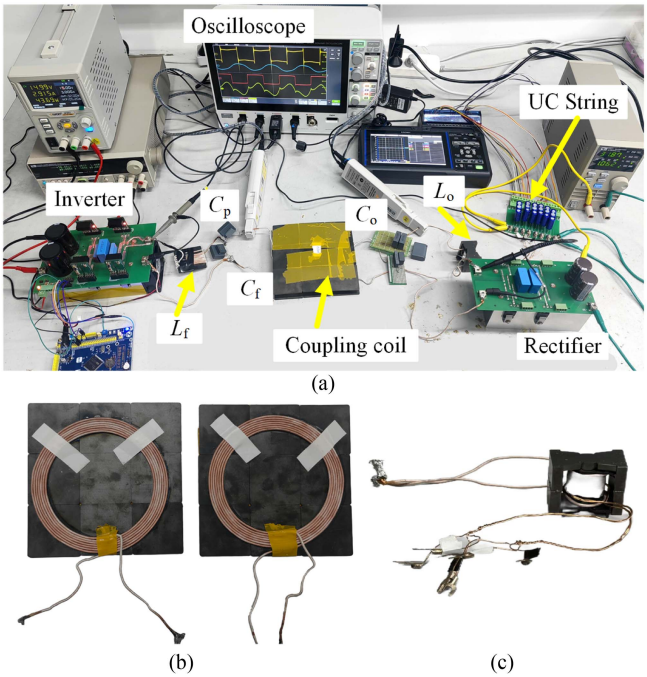

Fig. 6. Experimental platform of the proposed integrated equalizer for a UC string: (a) system overview, (b) identical transmitting and receiving coils, and (c) integrated transformer combining L_o with L_1–L_3, where the secondary windings consist of six taps formed by cowound enameled wires.

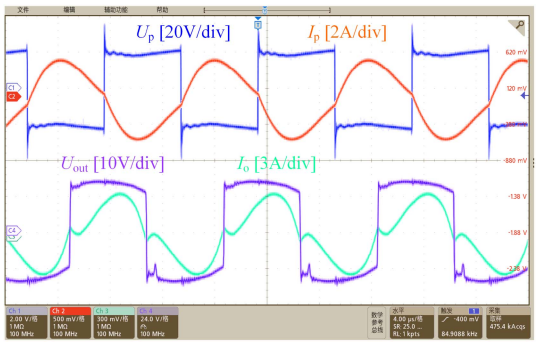

Fig. 7. Waveforms of U_p, I_p, U_{out}, and I_o in charging mode.

TABLE I
PARAMETERS OF THE INTEGRATED VOLTAGE EQUALIZER

Symbols	Parameters	Values
f	Operating frequency	85 kHz
U_{in}	Input voltage	6 V
U_{UCnm}	UC voltage of the nm cell	0–4 V
U_{UC}/U_B	Voltage range of UC/battery string	0–24 V
C_f	Compensation capacitor	274.8 nF
C_p	Compensation capacitor	270.6 nF
C_s	Compensation capacitor	142.2 nF
C_o	Compensation capacitor	144.5 nF
L_p	Transmitting coil	18.51 μH
L_f	Compensation inductance	12.56 μH
L_o	Compensation inductance	24.69 μH
L_s	Receiving coil	17.35 μH
M	Mutual inductance	9.90 μH
N_p	Number of turns of transmitting coil	7
N_s	Number of turns of receiving coil	7
L_1	Leakage inductance	0.70 μH
L_2	Leakage inductance	0.66 μH
L_3	Leakage inductance	0.69 μH
U_{Dn}	Diode voltage drop	0.22 V
N	Turns ratio	6:1
ϕ	Litz wire dimension	AWG 14 × 200
d	Transmission gap	2 cm

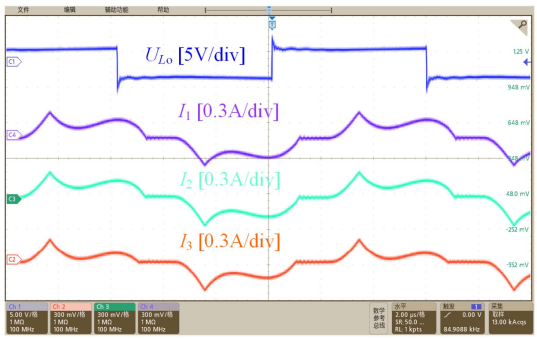

Fig. 8. Waveforms of U_{Lo}, I_1, I_2, and I_3 in balancing mode.

of individual energy storage cell voltages. For the battery-based experimental validation, the setup incorporated Camelion 18 650 lithium-ion batteries (2200 mAh). Table I details the pertinent parameters of the integrating voltage equalizer.

A. System Performance Under Various Initial Conditions

Figs. 7 and 8 illustrate typical operating waveforms of the proposed system. Fig. 7 depicts the WPT charging phase, showing the output voltage U_{out}, output current I_o, input voltage U_{in}, and resonant inductor current I_f. Fig. 8 highlights the balancing phase, presenting the voltage across L_o and the corresponding balancing currents I_1–I_3.

To evaluate the equalizer's performance under varying initial conditions, four test cases were conducted using UC cells. The corresponding results are shown in Fig. 9(a)–(d), where each subfigure illustrates the voltage balancing process for a distinct initial voltage distribution. In Case 1, cell voltages ranged from 2.1 to over 3.6 V, and the equalizer reduced the deviation to below 0.02 V within 50 s. Case 2 involved higher voltage levels with significant mismatches, while Cases 3 and 4 featured more complex imbalances, including high-voltage cells and uneven distributions. In all cases, voltage convergence was achieved within approximately 75 s, with the final deviation remaining below 0.02 V, demonstrating the equalizer's robustness across diverse imbalance scenarios.

To better reflect practical charging scenarios, battery cells were used in place of UC cells. As shown in Fig. 10, the initial cell voltages ranged from approximately 2.6 to over 3.3 V. Due to the higher capacity and slower dynamics of battery cells, the proposed equalizer required a longer balancing period, achieving convergence within 2000 s and reducing the maximum voltage deviation to below 0.03 V. Fig. 11 presents the measured overall system efficiency across output power levels from 10 to 25 W, where an efficiency of approximately 81.5% was achieved, indicating effective energy transfer under typical operating conditions.

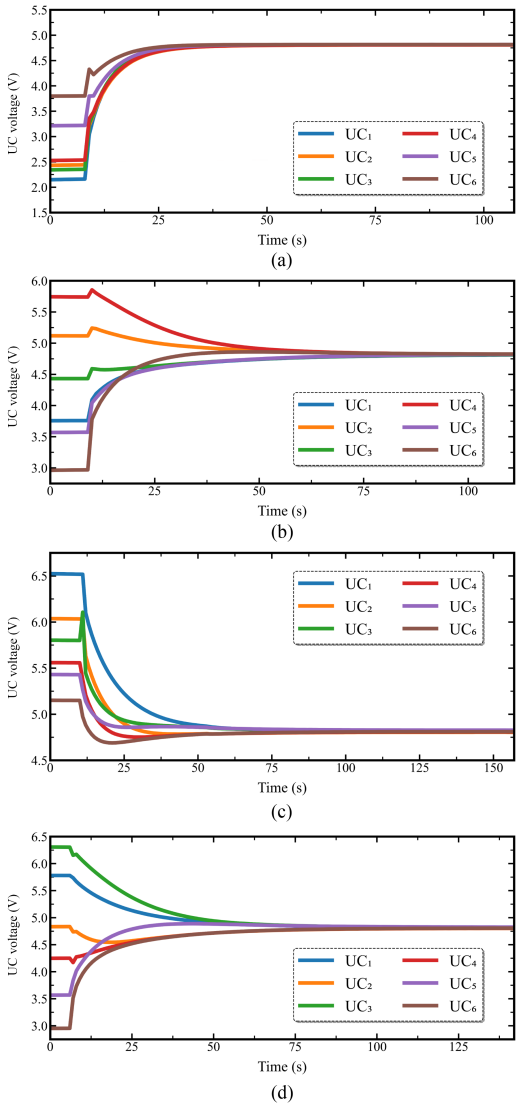

Fig. 9. Voltage balancing waveforms of the UC cells under four random initial voltage conditions. (a) Case1. (b) Case2.(c) Case3. (d) Case4.

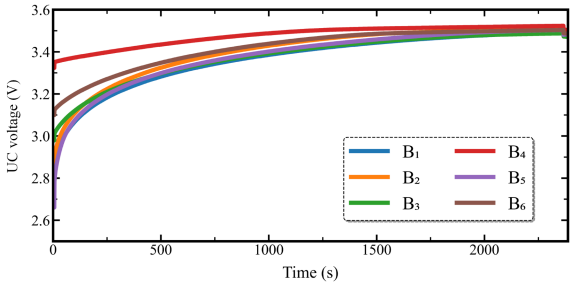

Fig. 10. Voltage balancing waveforms of battery cells with varying initial voltages.

B. Performance Under Coil Misalignment

To evaluate the resilience of the proposed equalizer to coil misalignment, experiments were conducted with a 40% displacement along the x-axis, which is representative due to the geometric symmetry of the coils. As shown in Fig. 12, despite this significant offset, the cell voltages converged smoothly within 200 s, reducing the initial voltage spread of approximately 0.3 to below 0.02 V. These results confirm that the equalizer maintains effective balancing performance under misaligned conditions.

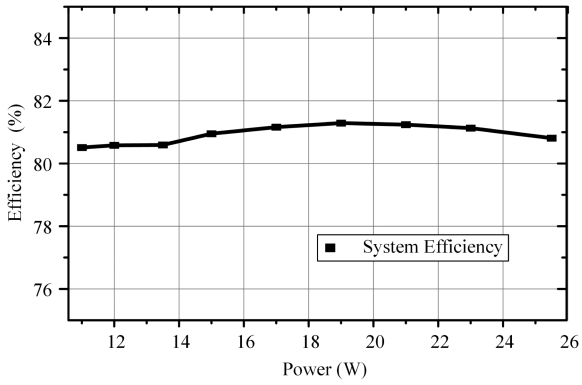

Fig. 11. Overall system efficiency with varying output power.

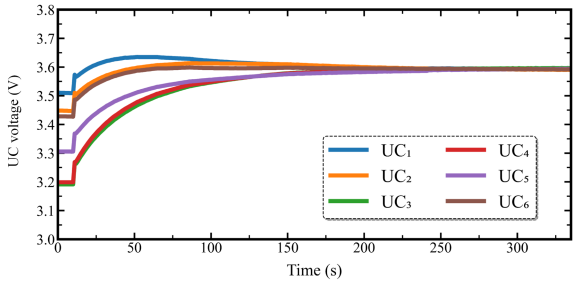

Fig. 12. Voltage balancing waveforms of the UC cells under 40% coil misalignment.

This robust performance arises from the transformer-based balancing mechanism, where the balancing voltage is determined solely by the turns ratio. Unlike multicoil architectures that are sensitive to coupling consistency under misalignment, the proposed design avoids such constraints by using a shared compensation inductor. This inherent decoupling from mutual inductance variations allows stable voltage convergence even under significant positional offsets, highlighting the simplicity and practicality of the topology for real-world WPT applications.

IV. Comparative Analysis and Discussion

Table II benchmarks the proposed equalizer against representative WPT-based balancing circuits using five metrics: simultaneous balancing capability, control logic (C-L) complexity, efficiency, and scalability. Performance levels—excellent (E), good (G), satisfactory (S), and moderate (M)—follow the rubric in [23]. Key observations are outlined below.

1) *Simultaneous balancing capability:* Unlike multireceiver topologies requiring one coil per cell, the proposed design utilizes each secondary winding to concurrently balance two cells. This enables rapid convergence for extended strings without duplicating receiver coils.
2) *C-L:* The proposed design employs a voltage-based, self-adaptive control strategy. This approach reduces hardware

TABLE II
COMPARISON OF WPT-BASED EQUALIZERS IN TERMS OF BALANCING PERFORMANCE AND FUNCTIONALITY

Balancing methods	Simultaneous	C-L	Efficiency	Scalability
Hybridized Ad-Hoc WPT equalizer [15]	G	Voltage-Based	76.4%	E
Multiple-receiver WPT equalizer [16]	G	Automatic	71.0%	M
Novel charging WPT Equalizer [18]	M	Voltage-Based	60.3%	E
Low-cost WPT equalizer [22]	G	Automatic	72.8%	M
Scalable cell-string WPT equalizer [23]	E	Automatic	76.5%	G
Proposed Equalizer	E	Automatic	81.5%	E

TABLE III
COMPONENT COUNT COMPARISON WITH REPRESENTATIVE UC-BASED EQUALIZERS

Components	[24]	[25]	[26]	[27]	[28]	[29]	Proposed
MOSFET	16	32	42	4	10	8	4
Inductor	0	0	2	1	9	8	2
Capacitor	0	15	5	32	21	24	4
Diode	0	0	4	64	32	32	20
Transformer	0	0	1	1	0	4	1
Coil	0	0	0	0	0	0	2
Resistor	16	0	0	0	0	0	0

complexity and permits adaptive balancing thresholds, resulting in lower cost and predictable control.

3) *Efficiency:* Regarding system efficiency, the proposed circuit achieves 81.5% . This is attained by routing energy through shared windings and limiting each equalization path to a single diode per cell, minimizing resistive losses.
4) *Scalability:* Regarding scalability, the proposed circuit demonstrates an excellent rating. Unlike multireceiver architectures requiring a dedicated coil per cell, adding two additional cells in the proposed design necessitates only one extra secondary winding and two diodes. This effectively halves the magnetic hardware requirement compared to baseline architectures, significantly simplifying integration for large-scale systems.

The proposed equalizer demonstrates the highest efficiency 81.5% among surveyed solutions. This performance, combined with its shared-inductor architecture, ensures excellent scalability. The design effectively eliminates redundant magnetic paths, leading to significant reductions in volume, cost, and misalignment sensitivity compared to multicoil systems. Furthermore, its self-adaptive voltage-based control simplifies implementation and facilitates precise regulation.

Table III offers a thorough economic viability assessment of the proposed equalizer by comparing it against a range of established topologies. The proposed architecture uses 33 components. While this is one more component than the design in [24], a closer look at the component types reveals a significant cost advantage: the proposed design only needs four MOSFETs, compared to the 16 used in [24]. This substantial reduction in high-cost active devices is key to its affordability. When benchmarked against other diverse topologies, which feature component counts ranging from 47 to 102, the proposed design stands out for its simplicity. The two coils are unique to the WPT architecture, enabling its distinct energy transfer process. In essence, the proposed equalizer boasts a highly economical component structure. Its minimal reliance on expensive active devices confirms its potential as a robust, low-cost solution ideal for various applications.

Despite these advancements, it is crucial to acknowledge the system's current boundaries. While the proposed topology was experimentally validated at 19 W with a charging efficiency of 81.5%, a key avenue for future investigation is scaling the system to medium power levels (e.g., up to 120 W). Such an enhancement would significantly broaden its range of potential applications but presents considerable challenges in thermal management and maintaining high efficiency, particularly within compact drone designs. Moreover, the current design primarily focuses on balancing during charging; extending self-balancing capabilities to active discharge cycles is another critical area for future refinement. These identified limitations are vital for framing the technology's current scope and directing future research efforts.

Ultimately, these combined attributes demonstrate the fundamental viability of the proposed topology. Addressing the aforementioned challenges will be paramount in realizing its full potential as a highly practical and scalable solution for integrated battery management in WPT-enabled systems, especially where compactness and robustness are required.

V. CONCLUSION

This article presents a WPT-based equalization topology that offers a compact, scalable, and robust solution. The cell balancing function is directly integrated into the receiver-side compensation network by reusing the compensation inductor as the primary of a multiwinding balancing transformer. This architecture eliminates bulky magnetic components and complex switching circuits, resulting in a simplified and compact

design. Accurate energy redistribution is achieved through turn-ratio control, and the system is inherently resilient to magnetic nonidealities, eliminating the need for tight parameter matching.

Experimental validation was conducted on both UC and battery strings, demonstrating reliable balancing performance. The system achieved an overall power transfer efficiency of 81.5% at 19 W output under simultaneous charging and balancing. Intercell voltage deviation was reduced to below 0.02 V. Notably, the equalizer maintained stable operation even under 40% coil misalignment, confirming its robustness for practical deployment. These results verify the effectiveness of the proposed architecture for high-performance, cost-sensitive WPT-enabled energy storage systems, especially in dynamic or mobile applications.

REFERENCES

[1] Y. Liu, H. Hu, X. Wang, Y. Gang, and Y. Li, "Voltage balance scheme for input-series output-series DAB DC–DC converter with bidirectional power flow," *IEEE Trans. Power Electron.*, vol. 39, no. 10, pp. 12030–12034, Oct. 2024.

[2] Y. Zou, H. Shi, W. Cao, S. Wang, S. Nie, and D. Chen, "A high-speed recurrent state network with noise reduction for multi-temperature state of energy estimation of electric vehicles lithium-ion batteries," *Energy*, vol. 322, 2025, Art. no. 135639.

[3] Z. Zhao et al., "Power electronics-based safety enhancement technologies for lithium-ion batteries: An overview from battery management perspective," *IEEE Trans. Power Electron.*, vol. 38, no. 7, pp. 8922–8955, Jul. 2023.

[4] R. Narayanan, J. Gangadharan, N. Sasidharan, and S. M. Pisharam, "A novel modularization method for voltage equalization of ultracapacitor bank using coupled inductor," *IEEE Trans. Ind. Electron.*, vol. 71, no. 4, pp. 3548–3558, Apr. 2024.

[5] G. Xu, E. Chen, F. Liu, Y. Liu, W. Xiong, and M. Su, "Multicell-to-multicell equalizer with hybrid pulsewidth modulation and phase-shift modulation," *IEEE Trans. Power Electron.*, vol. 39, no. 4, pp. 4400–4411, Apr. 2023.

[6] Y. Shang, C. Zhang, N. Cui, and C. C. Mi, "A delta-structured switched-capacitor equalizer for series-connected battery strings," *IEEE Trans. Power Electron.*, vol. 34, no. 1, pp. 452–461, Jan. 2019.

[7] Y. Ye, K. W. E. Cheng, Y. C. Fong, X. Xue, and J. Lin, "Topology, modeling, and design of switched-capacitor-based cell balancing systems and their balancing exploration," *IEEE Trans. Power Electron.*, vol. 32, no. 6, pp. 4444–4454, Jun. 2017.

[8] G. Zhou, X. Zhang, K. Gao, Q. Tian, and S. Xu, "Two-mode active balancing circuit based on switched-capacitor and three-resonant-state LC units for series-connected cell strings," *IEEE Trans. Ind. Electron.*, vol. 69, no. 5, pp. 4845–4858, May 2022.

[9] Z. Wei, F. Peng, and H. Wang, "An LCC-based string-to-cell battery equalizer with simplified constant current control," *IEEE Trans. Power Electron.*, vol. 37, no. 2, pp. 1816–1827, Feb. 2022.

[10] X. Tan, Y. Chen, J. Zeng, W. Liao, and J. Liu, "An integrated self-modularized battery equalizer and supercapacitor charger for hybrid electric vehicle energy storage system," *IEEE Trans. Veh. Technol*., vol. 73, no. 7, pp. 9865–9877, Jul. 2024.

[11] P. Cao et al., "Embedded lightweight Squirrel-cage receiver coil for drone misalignment-tolerant wireless charging," *IEEE Trans. Power Electron.*, vol. 38, no. 3, pp. 2884–2888, Mar. 2023.

[12] X. Yang, Y. Qi, J. Liu, Z. Jia, and D. Wang, "Bidirectional converter integrating voltage equalizer based on symmetrical voltage multiplier by sharing a magnetic component for series-connected cells," *IEEE Trans. Transp. Electrific.*, vol. 7, no. 3, pp. 1074–1087, Sep. 2021.

[13] Y.-H. Hsieh, T.-J. Liang, S.-M. O. Chen, W.-Y. Horng, and Y.-Y. Chung, "A novel high-efficiency compact-size low-cost balancing method for series-connected battery applications," *IEEE Trans. Power Electron.*, vol. 28, no. 12, pp. 5927–5939, Dec. 2013.

[14] L. Liu, Z. Yan, B. Xu, P. Zhang, C. Cai, and H. Yang, "A highly scalable integrated voltage equalizer based on parallel-transformers for high-voltage energy storage systems," *IEEE Trans. Ind. Electron.*, vol. 71, no. 1, pp. 595–603, Jan. 2024.

[15] P. Zhang et al., "Wireless charging of large-scale energy storage systems: A hybridized ad-hoc approach for high efficiency," *IEEE Trans. Power Electron.*, vol. 38, no. 11, pp. 13374–13383, Nov. 2023.

[16] M. Fu, C. Zhao, J. Song, and C. Ma, "A low-cost voltage equalizer based on wireless power transfer and a voltage multiplier," *IEEE Trans. Ind. Electron.*, vol. 65, no. 7, pp. 5487–5496, Jul. 2018.

[17] M. Liu, M. Fu, Y. Wang, and C. Ma, "Battery cell equalization via megahertz multiple-receiver wireless power transfer," *IEEE Trans. Power Electron.*, vol. 33, no. 5, pp. 4135–4144, May 2018.

[18] J. Sun et al., "A novel charging and active balancing system based on wireless power transfer for Lithium-ion battery pack," *J. Energy Storage*, vol. 55, 2022, Art. no. 105741.

[19] C. Hu, Z. Li, L. Kong, J. Wang, and C. Zhang, "Calculation method of mutual inductance of circular coils with bilateral convex toroidal magnetic medium in WPT system with horizontal misalignment," *Wirel. Power Trans.*, vol. 11, 2024, Art. no. wpt-0024-0004.

[20] Y. Feng, Y. Sun, T. Lin, H. Hu, and F. Chen, "Mutual inductance surrogate model of the UWPT system and its constant power optimization at misaligned positions," *Wirel. Power Trans.*, vol. 11, 2024, Art. no. wpt-0024-0001.

[21] P. Zhang et al., "Dual-layer equalization architecture for antimisalignment capability enhancement in multiple-receiver-based WPT equalizer," *IEEE Trans. Power Electron.*, vol. 39, no. 10, pp. 14027–1438, Oct. 2024.

[22] H. Feng, R. Tavakoli, O. C. Onar, and Z. Pantic, "Advances in high-power wireless charging systems: Overview and design considerations," *IEEE Trans. Transp. Electrific.*, vol. 6, no. 3, pp. 886–919, Sep. 2020.

[23] P. Zhang et al., "Wireless power transfer-based voltage equalizer for scalable cell-string charging," *IEEE Trans. Ind. Electron.*, vol. 71, no. 1, pp. 493–503, Jan. 2024.

[24] J. Gallardo-Lozano, E. Romero-Cadaval, M. I. Milanes-Montero, and M. A. Guerrero-Martinez, "Battery equalization active methods," *J. Power Sources*, vol. 246, pp. 934–949, 2014.

[25] Y. Shang, N. Cui, B. Duan, and C. Zhang, "Analysis and optimization of star-structured switched-capacitor equalizers for series-connected battery strings," *IEEE Trans. Power Electron.*, vol. 33, no. 11, pp. 9631–9646, Nov. 2018.

[26] X. Qi, Y. Wang, M. Fang, Y. Wang, and Z. Chen, "Principle and topology derivation of integrated cascade bidirectional converters for centralized charge equalization systems," *IEEE Trans. Power Electron.*, vol. 37, no. 2, pp. 1852–1869, Feb. 2022.

[27] X. Yang, L. Xi, Z. Gao, Y. Li, and J. Wen, "Analysis and design of a voltage equalizer based on boost full-bridge inverter and symmetrical voltage multiplier for series-connected batteries," *IEEE Trans. Veh. Technol.*, vol. 69, no. 4, pp. 3828–3840, Apr. 2020.

[28] M. Uno, D. Cheng, S. Onodera, and Y. Sasama, "Bidirectional buck-boost converter using cascaded energy storage modules based on cell voltage equalizers," *IEEE Trans. Power Electron.*, vol. 38, no. 1, pp. 1249–1261, Jan. 2023.

[29] M. Uno and K. Hasegawa, "Modular equalization system based on star-connected phase-shift switched capacitor converters with inherent constant current characteristics for electric double-layer capacitor modules," *IEEE Trans. Power Electron.*, vol. 35, no. 10, pp. 10271–10284, Oct. 2020.

Pengcheng Zhang (Senior Member, IEEE) received the B.S. degree in electrical engineering and the M.S. degree in control science and engineering from Tiangong University, Tianjin, China, in 2013 and 2016, respectively, and the Ph.D. degree in electrical engineering from the Hebei University of Technology, Tianjin, in 2021.

From 2017 to 2019, he was a Visiting Researcher with the School of Electrical and Computer Engineering, Georgia Institute of Technology, Atlanta, GA, USA. From 2021 to 2024, he was a Postdoctoral Researcher with the Department of Electrical Engineering, Tsinghua University, Beijing, China, where he is currently a Lecturer. His research interests include wireless power transfer and electromagnetic shielding.

Dr. Zhang was a Guest Associate Editor for IEEE TRANSACTIONS ON POWER ELECTRONICS and IEEE JOURNAL OF EMERGING AND SELECTED TOPICS IN POWER ELECTRONICS. He was the recipient of the First Place Prize Paper Award from IEEE Transactions on Power Electronics in 2022.

Tianhao Zhang is currentlyworking toward the B.Eng. degree in electrical engineering and automation with Sichuan University, Chengdu, China.

His research interests include battery management systems and wireless power transfer.

Xinjie Yu (Senior Member, IEEE) was born in Guizhou, China, in February 1973. He received the B.S. and Ph.D. degrees in electrical engineering from Tsinghua University, Beijing, China, in 1996 and 2001, respectively.

He is currently a Professor with the Department of Electrical Engineering, Tsinghua University. His current research interests include pulsed power supply, current sensors, computational intelligence, and wireless power transfer.

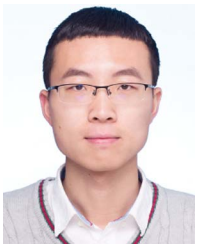

Zhaoyang Yuan (Member, IEEE) received the Ph.D. degree in electrical engineering from the Hebei University of Technology, Tianjin, China, in 2023.

From 2019 to 2021, he was a Visiting Researcher with the School of Electrical and Computer Engineering, Georgia Institute of Technology, Atlanta, GA, USA. He is currently a Postdoctoral Researcher with the Department of Electrical Engineering, Wuhan University, Wuhan, China. His research interests include engineering electromagnetism, wireless power transfer, and industrial applications.

Changsong Cai (Senior Member, IEEE) received the Ph.D. degree in electrical engineering from Wuhan University, Wuhan, China, in 2020.

From 2019 to 2020, he was a joint-cultivated Ph.D. Student with the School of Electrical and Computer Engineering, Georgia Institute of Technology, Atlanta, GA, USA. He is currently an Associate Professor with the School of Electrical Engineering and Automation, Wuhan University, Wuhan. His research interests include applied electromagnetics and power electronics, power conversion, wireless power transfer, magnetic design, and their industrial applications.

Dr. Cai was the Guest Associate Editor for IEEE TRANSACTIONS ON POWER ELECTRONICS. He was the recipient of a First Place Prize Paper Award from IEEE Transactions on Power Electronics in 2022 and an Outstanding Reviewer Award from IEEE Transactions on Power Electronics in 2024.

Hongjian Lin (Senior Member, IEEE) received the Ph.D. degree in electrical engineering from Southwest Jiaotong University, Chengdu, China, in 2021.

From 2018 to 2018, he was a Visiting Ph.D. Student with Energy Research Institute, Nanyang Technological University, Singapore. From 2019 to 2020, he was a Research Scholar with the School of Electrical and Computer Engineering, Georgia Institute of Technology, Atlanta, GA, USA. From 2021 to 2022, He was a Postdoctoral Research Associate with the Department of Electrical Engineering, Hong Kong Polytechnic University, Hong Kong. From 2022 to 2024, he was a Postdoctoral Research Fellow with the Department of Electrical Engineering, City University of Hong Kong, Hong Kong. He is currently a Postdoctoral Research Fellow with the Department of Electrical and Computer Engineering, University of Alberta, Edmonton, AB, USA. His research interests include predictive model control of converters in microgrids, electrical machines and drives control, magnetic component design, electric traction supply system, and modulation and control technologies of multilevel converters in the solid-state transformer.

Dr. Lin was an Associate Editor for IEEE OPEN JOURNAL OF POWER ELECTRONICS, and the Guest Associate Editor for IEEE TRANSACTIONS ON POWER ELECTRONICS andIEEE JOURNAL OF EMERGING AND SELECTED TOPICS IN POWER ELECTRONICS.

Yefei Xu (Member, IEEE) received the B.Sc. and M.Sc. degrees in electrical engineering from the School of Electrical Engineering, Shenyang University of Technology, Shenyang, China, in 2014 and 2017, respectively, and the Ph.D. degree in electrical engineering from the School of Electrical Engineering, Southwest Jiaotong University, Chengdu, China, in 2022.

He is currently an Associate Researcher with the School of Electrical Engineering, Sichuan University, Chengdu. His research interests include wireless power transfer and power cable defect location.

Lizhou Liu (Member, IEEE) received the B.S. degree in electrical engineering and the M.S. degree in control engineering from the Southwest University of Science and Technology, Mianyang, China, in 2014 and 2017, respectively, and the Ph.D. degree in electrical engineering from the School of Electrical Engineering, Southwest Jiaotong University, Chengdu, China, in 2021.

From 2021 to 2023, he was a Postdoctoral with Tsinghua University, Beijing, China. He is currently an Associate Research Fellow with the College of Electrical Engineering, Sichuan University, Chengdu. His research interests include energy storage technology, especially battery voltage equalizer, and hybrid energy storage technology.